Journal of Micromanufacturing, Volume 1, Issue 1, May 2018, pp. 6-19
DOI:10.1177/2516598418765359

Molecular dynamics simulation of the elliptical vibration-assisted machining of pure iron

Saurav Goel[1*], Fabian Duarte Martinez[1], Saeed Zare Chavoshi[2], Neha Khatri[3] and Claudiu Giusca[1]

[1]*School of Aerospace, Transport and Manufacturing, Cranfield University, Bedfordshire, MK430AL, UK*

[2]*Department of Mechanical Engineering, Imperial College London, London SW7 2AZ, UK*

[3]*Optical Devices & System Division, Central Scientific Instruments Organisation (CSIO), Chandigarh, 160030, India*

*Corresponding author Tel.: +44-1234-754132, Email address: saurav.goel@cranfield.ac.uk

Abstract:

It is well known that diamond wears out rapidly (within several meters of cutting length) when machining low carbon ferrous alloys and pure iron. The past few years have seen a growing interest in the field of elliptical vibration assisted machining (EVAM) due to it being successful in the micromachining of difficult-to-cut materials including steel. During EVAM, a cutting tool is prescribed an oscillatory motion perpendicular to the direction of cutting thereby causing the tool to be relieved intermittently from chemical and physical contact with the workpiece. This phenomenon served as a guideline to develop the simulation testbed for studying EVAM in this work to compare it with conventional cutting. The pilot implementation of the EVAM came as a Quasi-3dimensional (Q3D) elliptical cutting model of BCC iron with a diamond cutting tool using molecular dynamics (MD) simulation. The developed MD model supplemented by the advanced visualization techniques was used to probe the material removal behavior, the development of peak stress in the workpiece and the way the cutting force evolves during the cutting process. One of the key observations was that the cutting chips of BCC iron during conventional cutting became polycrystalline while EVAM resulted in cutting chips becoming highly disordered leading to better viscous flow compared to conventional cutting.

Keywords: MD simulation; elliptical machining; pure iron; tool wear.

Abbreviations:

1D VAM	1-Dimensional Vibration assisted machining
2D VAM	2-Dimensional Vibration assisted machining
ABOP	Analytical bond order potential
BCC	Body centred cubic
CAT	Crystal analysis tool (software program)
CBN	Cubic boron nitride
CAN	Common neighbour analysis
DMM	Ductile-mode machining
DXA	Dislocation extraction algorithm (software program)
EVAM	Elliptical vibration assisted machining
FCC	Face centred cubic
GSFE	Generalized stacking fault energy
HCP	Hexagonal close packed
LAMMPS	Large-scale molecular massively parallel simulator (software)
LCD	Liquid crystal display
μ-LAM	micro-Laser assisted machining
MD	Molecular dynamics
NVE	Microcanonical ensemble
OVITO	Open Visualization tool (software program)
PBC	Periodic boundary condition
PTM	Polyhedral template matching
Q3D	Quasi 3-Dimensional
RMSD	Root-Mean-Square Deviation
SDM	Surface defect machining
SPDT	Single point diamond turning
TWCR	Tool workpiece contact ratio
VAM	Vibration assisted machining

Nomenclatures:

A	Amplitude of vibration
b	Direction of Burgers vector
B	Vertical amplitude
C	Horizontal amplitude
C_{ij}	Elastic constants of the material
f	Frequency of vibration
Fx	Tangential cutting force acting on the tool in x direction
Fy	Thrust force acting on the tool in the y direction
t_c	Contact time between the tool and workpiece
r	Ratio of uncut chip thickness to cut chip thickness
t	The time taken by the tool to complete one cycle during cutting
u	Horizontal velocity of the tool
V_c	Cutting velocity
Vs	Nominal cutting speed
V_L	Maximum vibration velocity of the tool
ω	Angular velocity of the tool

1. Introduction

The term 'micromachining' refers to a special class of machining process wherein a small machined area of size (1 to 10^5) mm^2 is removed at a rate ranging from (10^{-5} to 1) $mm^3\ s^{-1}$ with an aim to

obtain an average surface roughness value not exceeding 100 nm [1]. Depending on the method of execution, micromachining can be categorized as mechanical (cutting, milling and grinding), physical (energy beam based machining methods) and chemical (photochemical machining, etching etc.) methods, each having their distinct advantages and limitations [2]. An important advantage of mechanical micromachining is that, apart from low carbon alloys, it can be applied to a wide range of engineering materials (metals, semiconductors, ceramics, optical glasses and plastics) to produce high precision non-rotationally symmetric and non-axisymmetric freeform surfaces for optical and electronic applications. The art of performing micromachining by making use of a diamond cutting tool forming an edge contact in the cutting zone along its radius is widely recognized as single point diamond turning (SPDT).

SPDT technology gained popularity for making high-speed polygon scanner mirrors (bar code readers, laser printers, etc.) and rolls for producing structured films, such as high reflectivity road signs [3], and for making non-optical components such as piston turning, boring, watch dials and other operations including hard disk drive heads [4]. SPDT is a popular choice for machining larger copper drums (used in Roll-to-Roll technology to prepare thin polymer films for large displays), diffraction gratings as well as for fabricating precision mirrors.

Consumer goods such as camera lenses, computer mice, barcode scanners, reflective tape, laser beam guiding systems or contact lenses, are mass produced by injection or compression moulding or by hot isostatic pressing, relying on the quality of diamond turned metal moulds [1]. As a tradeoff between cost and longevity for producing mass components, steel is the best engineering material with easy availability. This has elevated the necessity of machining steel moulds with high precision so that injection moulding of precision plastic optics can become a cost-effective manufacturing process. An ideal cutting tool material like diamond is chosen for micromachining due to its exceptional hardness (about 100 GPa), strong wear resistance, high thermal conductivity, and its ability to be sharpened down to a few nanometers (the edge radius can be of the order of 5 nm), but that is not enough: an intrinsically strong material can wear rapidly by simply changing the

counterface material or the sliding conditions. For instance, while machining iron or low carbon ferrous alloys: the high chemical affinity of carbon in iron leads to rapid degradation of diamond tool [5].

Various propositions suggests that the observed wear of the diamond tool can be divided into mechanical-abrasive wear (abrasion, microcracking) and chemical-reactive wear (diffusion, oxidation, catalytic graphitization and carbide-formation) or a combination of both [6]. The early postulation explaining the rapid wear of the diamond tool was proposed by Paul *et al.* [7] whereby the presence of unpaired *d-shell* electrons in the iron workpiece leading to gradual consumption of carbon from the diamond cutting tool was speculated. Subsequently, indirect experimental evidence [8] and a subsequent MD simulation study [9] proposed a mechanism of shear stress triggered diamond → graphitization leading to carbonization reaction with iron.

Attempts are made to mitigate the problem of tool wear and several innovations were proposed in recent years, which are reviewed elsewhere [10, 11]. Of these innovations, the one that has been particularly successful commercially to machine steel moulds is a hybrid micromachining technique called as ultrasonic elliptical vibration assisted machining (EVAM). To date, EVAM has been mostly studied experimentally and a level of understanding has been achieved, however, it is not properly understood how EVAM outperforms conventional cutting. What improvement does it bring and what is the mechanism of material removal during the process? A sound theoretical effort is required to find answers to these questions so that further improvement can be implemented through better insights of the EVAM process. This became the key motivation of the current paper- to compare EVAM and conventional cutting of iron where the tool is known to wear rapidly.

The work presented in this paper was performed taking a bottom-up fundamental simulation approach using molecular dynamics (MD) simulation. MD has been particularly successful in addressing precise aspects of materials science that are otherwise difficult to explain with any other simulation or experimental methods. The BCC iron was chosen deliberately as the workpiece material as it would allow for highlighting the advantages of EVAM (if any) over conventional

machining within the limited length scale of the MD simulation. As a by-product of this investigation, the paper aims to provide answers to the following open questions which will aid to understand and improve the EVAM process even further:

1. How do the cutting forces vary during conventional cutting and during elliptical path cutting?
2. How does the material removal mechanism differ between conventional machining and elliptical path machining?
3. How do the thermodynamic conditions i.e. flow stress and cutting temperature differ in the two cases and do they both evolve in the same way or differently?
4. Most noticeably, does the elliptical path movement shows some wear protection of the diamond cutting tool within a few nanometers of cutting while using iron as workpiece?

The rest of the paper is organised detailing the literature and discussing the results obtained from the MD simulation. Section 2 provides a detailed review of the elliptical vibration assisted machining process and section 3 shows the implementation of the research methodology using the MD algorithm with a comparison of the potential functions employed in this study. Based on the assessment of the potential functions and the subsequent simulation results, Section 4 presents the novel findings highlighting the differences in the evolution of cutting forces, yield stresses, origins of ductile plasticity during conventional cutting and EVAM, dislocation nucleation behaviour and some insights showing the EVAM process to be a strategy for wear protection of the diamond tools.

2. VAM and EVAM

The literature refers VAM as the process of intermittent cutting. The reported benefits include low wear rate of the tool, reduce burr formation on the workpiece and achieving higher depths especially for ductile-regime machining [12] of brittle materials like silicon. The attainable cutting speeds during VAM are limited by the hardware and system and hence ultrasonic assisted machining methods are classed as low speed machining techniques [13]. Also, the process of vibration assistance can be implemented in two ways (i) uniaxial tool movement (1D VAM) where

the tool vibrates in a plane parallel to the surface of the workpiece; and, (ii) elliptical tool movement [14] – EVAM, where the tool vibrates with an elliptical motion. Both methods can be resonant based and non-resonant based. The resonant system operates at discrete frequencies, normally higher than 20 kHz and amplitudes less than 6 µm, whereas, the non-resonant system operates at a between (1 to 40) kHz and amplitudes ten times higher than the resonant system. Recent research effort shows that the tool movement with a frequency of about 80 kHz in the cutting direction reduces the wear of the diamond tool by one hundred times or more [14].

During the infancy phase, the toolpath was modified by adding an amplitude and frequency to the displacement of the tool and this was referred to as 1D VAM. Figure 1 provides an illustration of the tool movement and variation in cutting force in 1D VAM compared to conventional machining.

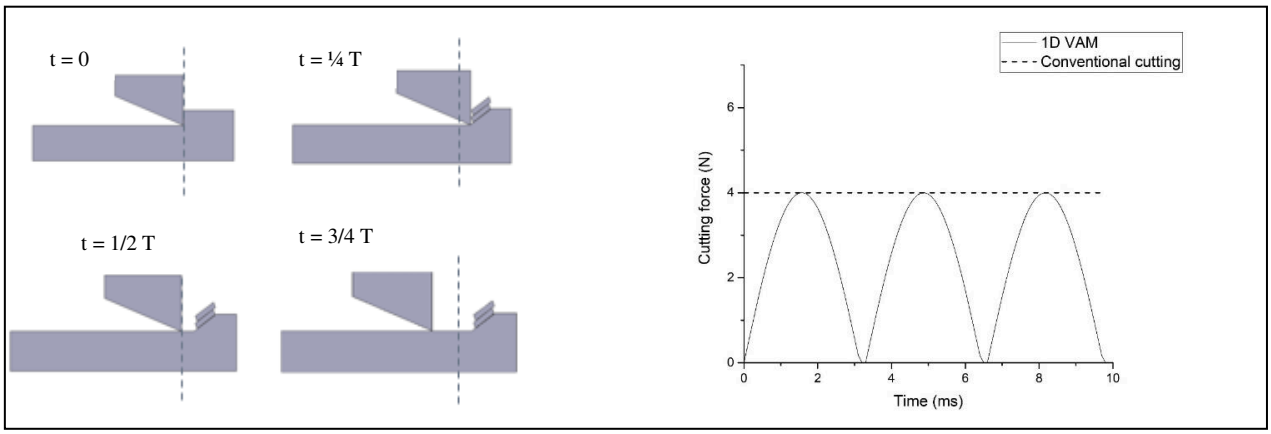

Figure 1: (a) Schematic diagram depicting various stages in 1D VAM and (b) a sample plot showing a comparison in the evolution of cutting force in 1D VAM and conventional machining

As can be observed in figure 1, whilst the peak value of the cutting force is the same in both conventional cutting and 1D VAM the oscillation causes the average cutting force in 1D VAM to be significantly less. During 1D VAM, the tool loses contact with the workpiece in a periodic fashion, therefore the tool is separated from the primary and secondary shear zones for frequent intervals during each cutting cycle. This provides an advantage of reduced tool wear and enables the cutting of materials with low thermal conductivity and high heat capacity such as titanium alloys [15].

An important term in VAM is tool workpiece contact ratio (TWCR) which can be described as follows:

$$TWCR = \frac{t_c}{t} \quad (1)$$

where t_c is the contact time and t is the time it takes the tool to complete one cycle during cutting. TWCR refers to the ratio of the time that the tool is in contact with the workpiece and the time it takes the tool to complete one vibration cycle. Several reports suggest that decreasing TWCR decreases the cutting forces significantly. It has also been reported that increasing the amplitude and frequency leads to a lower TWCR and hence a reduction in cutting forces. Sharma et al [16] tested different amplitudes and frequencies to obtain optimum machining conditions during ultrasonic assisted turning. For instance, by maintaining constant frequency and by increasing the amplitude up until a critical value, cutting forces were observed to decrease. An additional consideration is that the maximum vibration velocity of the tool should be equal to or higher than the cutting speed. This scenario can be presented by equations $v_{\max} \geq v_c$ and $\omega A \geq v_c$ where $v_{\max}$ is the maximum vibration velocity of the tool, A is the amplitude, ω is the angular velocity of the tool and v_c is the cutting speed.

The limitations of 1D VAM resulted in a further advance which is referred to as 2D VAM or simply EVAM. In this technique, the tool vibrates in two dimensions (2D) to form an elliptical path. EVAM brings about reversal of the direction of friction and an improved plasticity by the virtue of enhanced shear angle [17]. In general, the machining or the cutting forces are divided into two components, i.e. friction force (tangential cutting force) along the x direction and normal force (thrust force) along the y direction. Friction forces are a result of the frictional contact between the rake face of the cutting tool and the cutting chips.

The main advantage of EVAM over 1D VAM is that friction forces are significantly reduced and this decreases the average forces during machining. The reduced friction forces are associated with the vertical vibration velocity of the tool. The pioneering work by Moriwaki and Shamoto [18-20] highlights these advantages and suggests that the elliptical tool movement results in an improved chipping of the material and reduced cutting forces.

Table I provides a schematic illustration of the toolpath of EVAM. The major axis of the ellipse is in the same direction as the cutting force and the minor axis of the ellipse is along the direction of the thrust force. The tool vibration velocity varies both in vertical and horizontal directions from zero to a maximum and achieves different values at different points in the tool path shown in table II. The equations shown in table I describe the vertical and horizontal displacements of the tool with respect to time and the maximum horizontal and vertical components of velocity.

Table I: Equations describing the toolpath during elliptical vibration assisted machining (EVAM)

Schematic representation highlighting stages in toolpath during 2D VAM (EVAM)	**Variable**	**Equation**
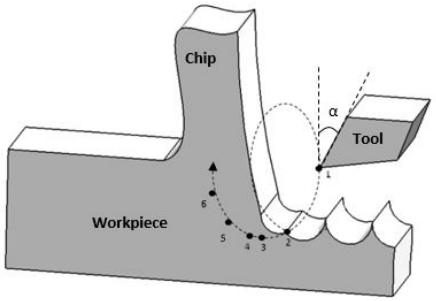 1: Initial point 2: Beginning of cutting 3: Lowest vibration point 4: Contact between chip and workpiece 5: Reverse in the direction of friction 6: End of cutting α: Rake angle	Vertical displacement	$S_y = -B\cos(\omega t)$
	Horizontal displacement	$S_x = ut + C\sin(\omega t)$
	Maximum horizontal vibration velocity	$vx_{\max} = C\omega$
	Maximum vertical vibration velocity	$vy_{\max} = B\omega$
where C is the horizontal amplitude, B is the vertical amplitude, u is the horizontal velocity of the tool and ω is angular velocity = $2\pi f$ (where f is frequency). Also, V_L (largest vibration speed = $2\pi Cf$) > Nominal cutting speed (Vs)		

Table II: Velocity of the tool at horizontal and vertical position at different instances during EVAM

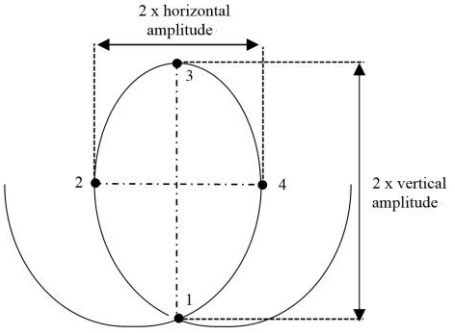	**Position**	**Horizontal vibration velocity**	**Vertical vibration velocity**
	1	Maximum	Zero
	2	Zero	Maximum
	3	Maximum	Zero
	4	Zero	Maximum

During the initial stage of the cutting period, the vertical vibration speed in EVAM is lower than the speed of the chip flow. This causes friction between the chip and the rake face tool, which consequently leads to the chip being pushed down. However, when the vertical vibration speed of the tool exceeds the speed of the chip flow, the tool is pulling the chip is upwards, causing an effect

known as reversed friction. It was also reported that the average frictional force over many cycles acts in an opposite direction as the chip is driven by the rake face of the tool [19]. This “reversed friction force” leads to lower cutting forces, lower chip thickness, suppresses the generation of burrs and enables higher shear angles compared with 1D VAM thus making EVAM (2D VAM) superior to VAM (1D VAM). During the final stage of the elliptical motion, the tool moves down without cutting, therefore it comes out of contact with the chip. For instance, Ma *et al.* [21] reported that the height of burrs in EVAM is fifteen times lower than in VAM when working with Aluminium (52S), which has a significant impact in machining time and cost involved with deburring processes. Shamoto *et al.* [22] reported that increasing the frequency of EVAM leads to an increased shear angle.

Astashev et al. [23] reported that a vibrational frequency during cutting causes a transformation of elasto-plasticity into visco-plasticity. In addition, it causes the fluidization of dry friction or the dry friction in the contact region between the tool and the workpiece transforms into viscous friction bringing a substantial decrease in flow stress of the material. Brinksmeier [24] used EVAM to study the relationship between the effective contact time and tool wear. They measured the tool life in terms of the cutting distance at which the surface roughness of the tool dropped below 40 nm (RMS). They reported an increase in tool life cutting length from 0 to 20 m when decreasing the effective contact time from 52 % to 22 %. Yang et al. [25] reported notable improvements in this area as they achieved vertical and horizontal amplitudes of 12 µm and 4.5 µm. Table III gives a ready idea of efforts made both in 1D VAM and EVAM for the past seven years and the reported level of improvements made. As evident from table III, the majority of studies show less wear and improved surface roughness.

Table III: Tabulated summary of recent efforts made in VAM of titanium alloys and steel

Work material	Cutting parameters used	Oscillation parameters (frequency (f), amplitude (a))	Cutting force comparison with conventional turning	Additional conclusions
Ti6Al2Sn4Zr6Mo (α+β Ti alloy) [26]	f_r = 0.1 mm/rev; v = 10-60 m/min; d = 0.2mm	f = 20kHz; a = 10 µm	Reduction by 74%	Surface roughness improved by 50%
Ti-15333 (β alloy) [27]	f_r = 100 µm/rev; v = 10m/min; d =100-500 µm	F = 20 kHz a = 8 µm	Reduction by 80-85%	Surface roughness improved by 50% while heat was applied during ultrasonic assisted machining
Ti6Al4V [28]	f_r = 0.1mm/rev; v = 10-300m/min d = 0.1mm	f = 20 kHz a = 20µm	Reduction by 40-45%	Surface roughness improved by 40%
Ti 15-3-3-3 (β Ti-alloy) [29]	F_r = 0.1mm/rev; v = 10-70m/min; d = 50-500 µm	f = 17.9 kHz a = 10 µm	Reduction by 71%-88%	Surface roughness improved by 49%
Low alloy steel (DF2) [30]	F_r = 0.1mm/rev; v = 50m/min; d = 0.2mm	F = 19 kHz; a = 15 µm	Reduction by 50%	Tool wear 20% less.

New frontiers in EVAM will arise once the high power elliptical vibrators can operate at higher frequencies and higher vibration amplitudes [31]. One of the currently researched areas is to use ultrasonic frequencies, which will enable the manufacture of gratings of 10 µm pitch on materials such as aluminum.

The literature also shows preliminary attempts of carrying out MD simulation of EVAM [32, 33] detailing some of the salient aspects of the method, however, it is such a fertile area of research that a lot more is yet to be investigated especially on the mechanisms behind tool wear suppression and plasticity improvements during EVAM. More recently, efforts are made in studying plasticity of iron during contact loading [34-36]. The focus of these studies was primarily to study the plasticity in the iron substrate, so the diamond tool was either considered rigid or was modelled with a hypothetical potential. Therefore, this work uses a full parameterized potential function for iron and carbon to show insights into the chemical interaction and to model realistic forces for a better comparison of EVAM with conventional cutting of iron with a diamond cutting tool. One may note that the experimental conditions often involve the presence of a chemical (e.g. Oxygen or nitrogen) environment, which leads to the formation of a surface layer, while in our MD simulations we model pure iron. This aspect, however, turned out to be fortuitous for this study as it makes the

performance of the machining insensitive to the presence of the environment. In view of this consideration, the results of this study may be viewed only as a testbed study performed in a vacuum.

3. Molecular dynamics simulation methodology

In this work, the "Large-scale Atomic/Molecular Massively Parallel Simulator" (LAMMPS 17th November 2016 version) [37] was used to perform a series of MD simulations. OVITO [38] was used to visualize and analyse the atomistic simulation data while an automated "dislocation extraction algorithm" (DXA) [39] and crystal analysis tool (CAT) [40] were used for automated identification of crystal defects, dislocation lines and their Burgers Vector from the output of the MD data.

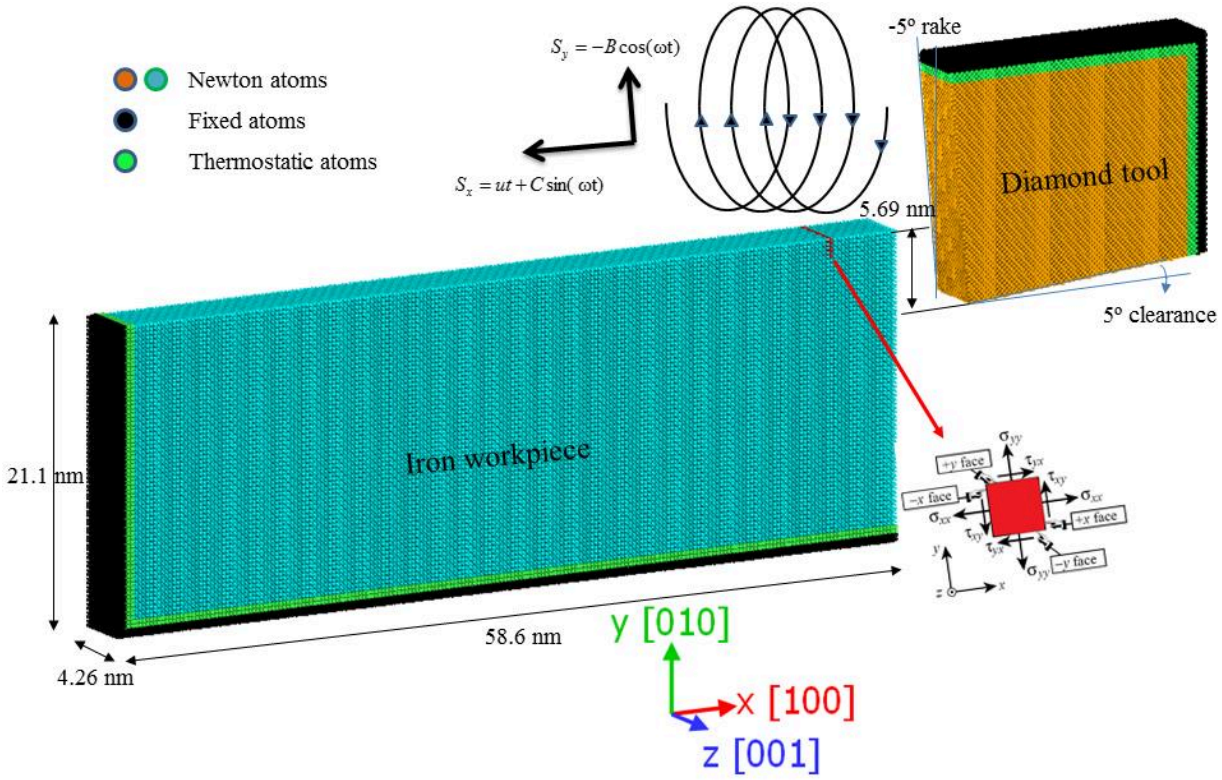

Figure 2: Schematic diagram of the MD simulation model of the nanometric cutting of iron. A small volume of material (red group of atoms of dimension 0.36 nm × 1.42 nm × 4.27 nm (~135 atoms)) was used to monitor the stress evolution in the cutting region. Yellow atoms are Newton atoms within the crystalline diamond cubic atoms while blue atoms Newton atoms in the BCC iron workpiece. The outer peripheral boundaries showing black and green shaded atoms, both in the tool and the workpiece, are that of fixed boundaries and thermostatic regions*

The MD simulation model after initial equilibration is shown in figure 2. Atoms of the workpiece (BCC Fe atoms) and those of the diamond cutting tool (carbon atoms) were divided into three distinct zones, namely boundary atoms, thermostatic atoms and Newton atoms. The atoms in the Newton region, which is directly affected by the tool-workpiece interaction, followed Newtonian dynamics (NVE dynamics), while atoms in a thin boundary layer were subjected to a thermostat to dissipate the heat generated in the cutting region, which, in experiments, is dissipated by air or lubricant. Atoms at the outermost boundary of the model were fixed to keep the workpiece in place, while boundary atoms of the cutting tool were rigidly moved at a constant velocity. Prior to carrying out the cutting simulations in this work, various potential functions available in the literature were tested for their accuracy in reproducing the elastic constants and other important mechanical properties such as Zener anisotropy ratio, Young's modulus, shear modulus, Voigt Poisson's ratio and the Voigt Bulk modulus of iron. The values of these parameters are shown and compared with experiments in table IV for reference.

Table IV: Experimental properties of iron compared with the values obtained from the MD simulation at 0 K using different types of potential energy functions

Properties of iron obtained from MD compared with experiments	**ABOP [41, 42]**	**EAM [43]**	**MEAM 2NN [44]**	**Experiment [45]**
Equilibrium lattice constant (**Å**)	2.8602	2.8553	2.8637	2.87
$C_{11} = C_{22} = C_{33}$ (GPa)	225.009	244.47	242.979	243.1
$C_{12} = C_{13} = C_{23}$ (GPa)	141.822	146.17	137.99	138.1
$C_{44} = C_{55} = C_{66}$ (GPa)	128.43	116.22	121.918	121.9
Zener anisotropy ratio $\frac{C_{11}-C_{12}}{2\times C_{44}}$	0.32	0.42	0.43	0.43
Young's modulus (E_{100}) [46] (GPa) $C_{11}-2\frac{C_{12}}{C_{11}+C_{12}}C_{12}$	115	135	143	143
Young's modulus (E_{110}) [46] (GPa) $4\frac{(C_{11}^{\ 2}+C_{12}C_{11}-2C_{12}^{\ 2})C_{44}}{2C_{44}C_{11}+C_{11}^{\ 2}+C_{12}C_{11}-2C_{12}^{\ 2}}$	217	224	234	234
Young's modulus (E_{111}) [46] (GPa) $3\frac{C_{44}(C_{11}+2C_{12})}{C_{11}+2C_{12}+C_{44}}$	308	287	296	296
Shear modulus(G) [47] (GPa)	70.5	71.5	75.6	75.6

* Readers are requested to refer the web based version of this article for correct interpretation of the colour legends

$\frac{C_{11}-C_{12}+C_{44}}{3}$				
Shear Strength (G/2π) in GPa	11	11	12	12
Voigt Poisson's ratio [47] $\frac{C_{11}+4C_{12}-2C_{44}}{4C_{11}+6C_{12}+2C_{44}}$	0.27	0.29	0.27	0.27
Voigt Bulk Modulus(B) (GPa) [48] $\frac{(C_{11}+C_{22}+C_{33})+2(C_{12}+C_{13}+C_{23})}{9}$ or $\frac{(C_{11}+2C_{12})}{3}$ for isotropic	170	179	173	173

It is evident that all the potentials tested can fairly reproduce the mechanical properties of iron however, carbon was only parametrised in the ABOP [41, 42] potential and not with the EAM [43] and MEAM 2NN [44] potentials. For instance, the equilibrium lattice constant of diamond obtained from these potentials were 3.5575 Å, 3.9305 Å and 5.355 Å with the ABOP, EAM and MEAM 2NN potentials respectively. This implies that only fully parameterised potential function, ABOP, could be used in the simulation. While an option of a hybrid scheme i.e. combining two potential functions is feasible, it carries implications that must be fully understood before the implementation of combining two different types of many-body potential functions. It may further be noted that pure iron exhibits a phase transition between BCC α-iron and FCC γ-iron at a temperature of about 1184 K, and the martensitic phase of FCC γ-iron undergoes a reverse transition back to the BCC phase (δ-iron) at about 1665 K before undergoing melting [49]. The melting point of BCC iron (at zero pressure) predicted by the ABOP potential is roughly about 2270 K as opposed to an experimental value of about 1811 K [49, 50]. Most of the potential functions, specifically bond order potentials predict a melting point of the bulk material by tens of percent out of the experimental value and this is therefore an acceptable and reasonable prediction. The results comparing the performance of various potentials in predicting the phase diagram of iron is available from a recent PhD thesis [51]. Considering these comparisons, ABOP was selected as the preferred potential in this study for simulation of both iron as well as carbon as it was fully parameterised for both of these atomic species. Further details of the MD simulation model are shown in Table V for the purpose of reproducibility.

Table V: Process variables and details of the MD simulation model

Workpiece dimensions	58.6 nm × 21.1 nm × 4.26 nm	
Number of atoms	Iron workpiece = 455,100	Diamond tool = 221,388
Uncut chip thickness (*d*)	5.69 nm	
Workpiece cut surface and cutting direction	(0 1 0) and <100>, Cutting was performed at 300K in NVE ensemble	
Fe-C interatomic potential function	Analytical bond order potential [41] as implemented previously during nanoindentation study [52]	
Cutting tool (rake and clearance angle)	(-5° and 5° respectively) and extremely sharp edge (deformable)	
Cutting distance (free travel + cutting length)	(6+39) nm=45 nm	
Velocity of the tool (Nominal cutting speed of the tool) (*Vs*)	150 m/s = 0.15 nm/ps	
Total simulation time	45 nm/ 0.15 nm/ps = 300 ps	
MD Timestep	0.5 fs = 0.5×10^{-3} ps	
Total run timesteps	300/0.0005 = 6,00,000	
Additional parameters for EVAM simulation	Vibration frequency (f) = 400 GHz, Amplitude in X (C) and Y direction (B) = 1 Å V_L (largest vibration speed = $2\pi Cf$ = 251.3 m/s) > Nominal cutting speed (Vs) of 150 m/s	

4.0. Results and discussions on EVAM and conventional cutting

4.1. Analysis of cutting forces, yielding stresses and dislocation mediated plasticity in iron

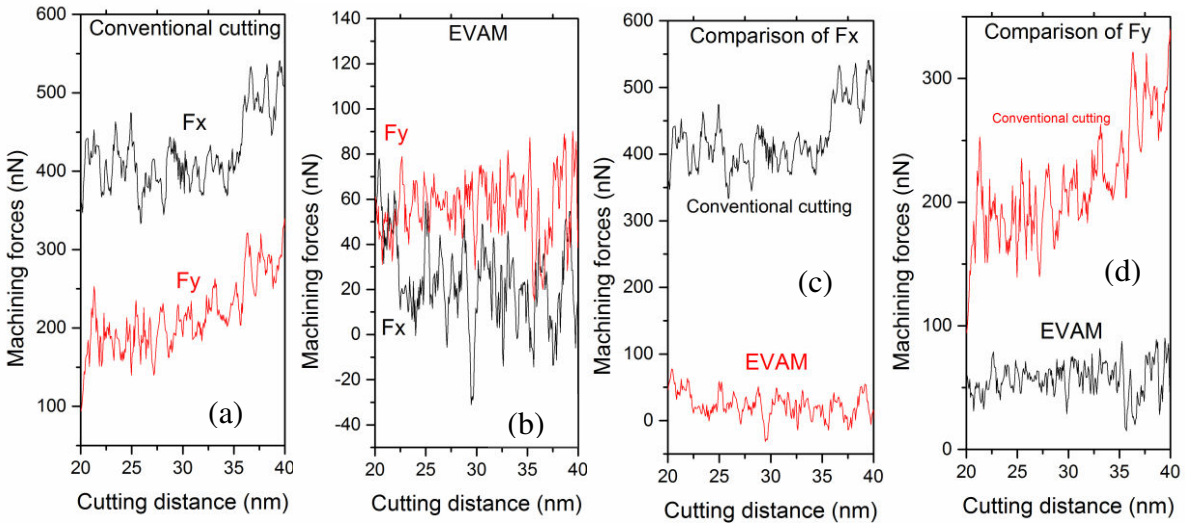

Figure 3: Comparison of machining forces (a) *Fx* and *Fy* during conventional cutting (b) *Fx* and *Fy* during EVAM (c) *Fx* compared during conventional cutting and EVAM and (d) *Fy* compared during conventional cutting and EVAM

Figure 3 (a) and Figure 3(b) shows the evolution of friction force (tangential cutting force) along the *x* direction and normal force (thrust force) along the *y* direction during conventional cutting and EVAM. Figure 3(c) and Figure 3(d) are comparisons of *Fx* and *Fy* for the two types of cutting

processes simulated in this work. The large noise in the cutting force signal reflects the discontinuous nature of material removal and a number of events occurring due to the tool-workpiece interactions including initiation of the wear of the tool, dislocation nucleation and propagation and continuous change of the shear plane angle. A stark observation that came to light from comparing the cutting forces is that the EVAM process leads to a significant reduction in the forces. A summary of force results in tabulated in Table VI. It may also be seen that the value of the kinetic coefficient of friction is reduced tremendously from 1.96 to 0.4 while using EVAM as opposed to conventional cutting. These values provide quantitative indications of the level of performance improvement achievable during the EVAM process.

Table VI: Summary of results of cutting forces and Coefficient of kinetic friction

Measurement of forces and friction	**Conventional cutting**	**EVAM**
Thrust force (Fy) in nN	216	57
Cutting force (Fx) in nN	423	23
Kinetic coefficient of friction (Fx/Fy)	1.96	0.4

An application of force during machining brings about yielding in the material and it is important to quantify the equivalent stress measure that causes this yielding. A widely held view on nanoscale plasticity is that von Mises and Tresca stress measures are more suited to predict yielding in ductile materials whereas the Principal stress criterion is more suited to predict yielding in brittle materials. Indeed, for a brittle material like silicon, the Principal stress criterion was found to be reasonably appropriate in the prediction of yielding during cutting [53]. As for iron, this work aims to examine the appropriate yield criterion during conventional and EVAM cutting and the obtained results are shown in Table VII. It may be seen that a von Mises stress of about (6 to 7) GPa or a Tresca stress of about (3 to 3.5) GPa can bring about yielding in BCC Fe. During the simulations it was observed that the yielding process was accompanied by a metastable (BCC to FCC and HCP) phase transformation of iron which will be further explored later. At this point, it is also imperative to note that the von Mises stress peak on the diamond cutting tool while cutting iron remained typical of the order of (15 to 20) GPa.

Table VII: Nanoscale yielding stresses of iron and forces on the diamond cutting tool iron observed during the cutting simulation

Stress peak (GPa) causing nanoscale yielding of iron	**Conventional cutting**	**EVAM**
Von Mises stress	5.9	7.1
Octahedral shear stress	2.8	3.4
Tresca stress	3.4	4
Major principal stress	2.7	0.17
Minor principal stress	-4	-8

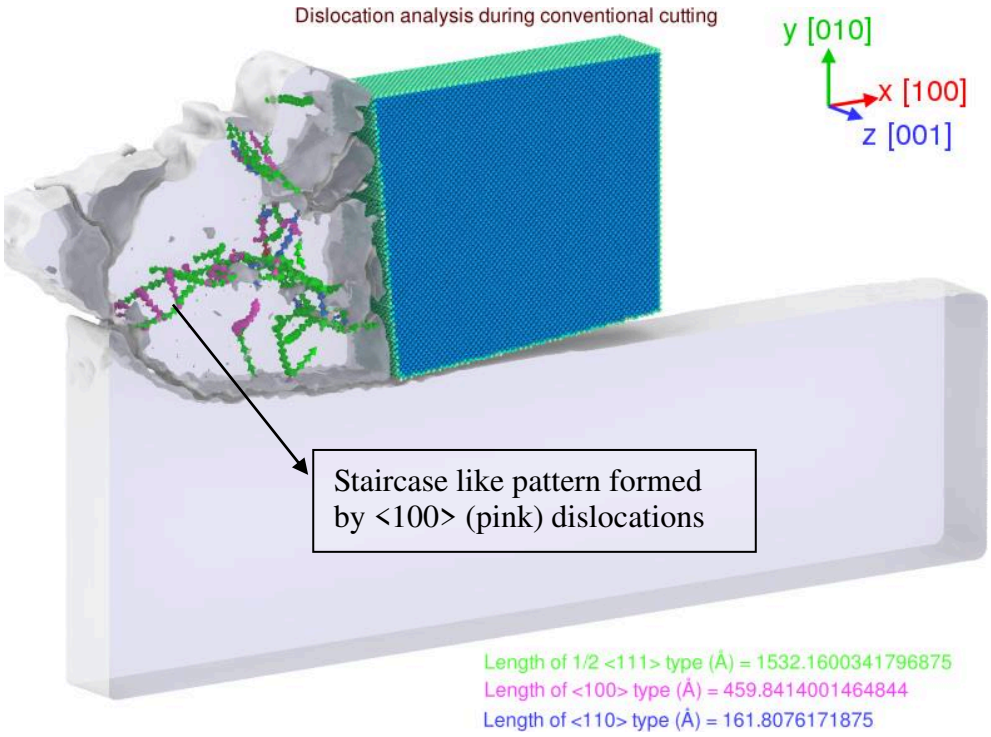

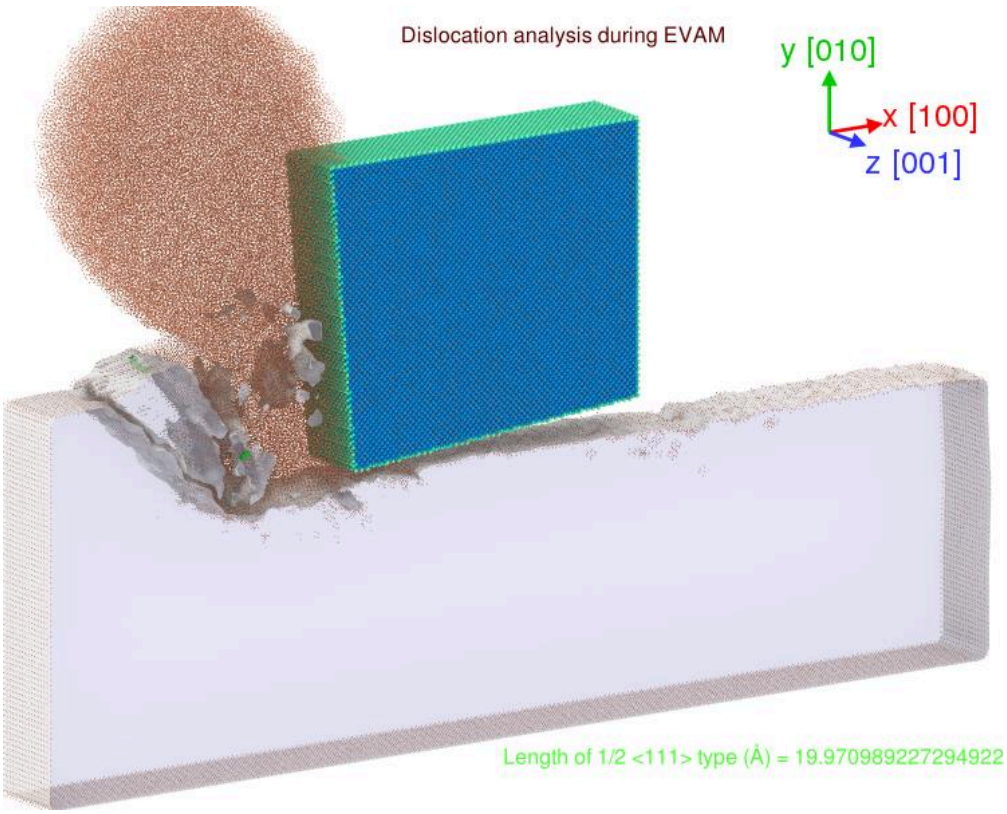

Figure 4: Comparison of dislocation structures in iron during conventional cutting and EVAM. These views are obtained from DXA processing showing distinct plastic deformation zone and free surface for enhancement in the visualization. The brown atoms are that of the unidentified crystal structure while Dislocations with **b**=1/2<111> are shown in green, **b**= <100> are shown in pink and **b**= <110> are shown in blue respectively

After analysing the cutting forces and yield stresses, their consequence on the material’s plastic behaviour was studied. For example, prior to the investigation of this work, it was not known whether the ductile plasticity occurring in pure BCC iron during cutting is due to dislocation nucleation, shear band propagation or other phenomena such as phase transition. To this end, figure 4 shows images and views of an instance during the cutting process analysed from the DXA process. The simulation snapshots reveal differences in the material plasticity during conventional cutting and during EVAM which are summarised in table VIII.

Table VIII: Summary of results showing crystalline defects and dislocations type

Cutting Scenario	Nature of chip formation	Dislocation type
Conventional cutting	Identified small crystallites of iron with grain boundary separation. Three types of dislocations were observed to be the plasticity carrier responsible for material transport	**b**=1/2<111>, **b**=<100> and **b**=<110>
EVAM	Unidentified crystal structure	Very small dislocation segment of **b**=1/2<111> type

As anticipated the ductile plasticity in cutting pure iron using conventional method was observed to be due to the dislocation nucleation and propagation. Broadly, three major types of dislocations with Burgers vectors **b**=1/2<111> (green colour), **b**=<100> (pink colour) and **b**= <110> (blue colour) were revealed in the cutting chips and not in the workpiece while performing conventional cutting. This alludes to the fact that the crystalline cutting chips flow more easily on the tool's rake face by the virtue of plasticity induced by the dislocations, however, the <100> dislocations were observed to emerge from the interaction between two 1/2<111> types and resembled stair-rod patterns as highlighted in figure 4. These dislocations are immobile and slows down the flow rate of the cutting chips during cutting of single crystal BCC Fe by conventional means.

By and large, the three dislocations highlighted above were observed to be accompanied by continuous movement of the shear plane such that the chips retain crystalline BCC structure. Consequently, the nature of chip removal and cutting chips during conventional cutting was associated with removal of iron in small crystallites having their BCC structure and overall the cutting chips seemed to be polycrystalline nature. Thus, these chips were the carrier of material causing transport of plasticity in pure iron during conventional cutting. Contrarily, the mechanism of plasticity during EVAM differed significantly compared to conventional cutting. For instance, a very small dislocation segment of **b**=1/2<111> (green colour) was observed in the cutting chip ahead of the viscous flow of pure iron. This viscous flow was totally absent during cutting of iron with the conventional method. As opposed to dislocation mediation, the cutting chips (brown atoms) during EVAM remained unidentified from the DXA tool, requiring further inspection as

discussed in the next section. It may however be noted that the dislocation slip in BCC metals is directly associated with certain fault energies i.e. generalized stacking fault energy (GSFE) on three slip planes: [110], [112], and [123]. The ABOP potential overestimates the relaxed unstable stacking fault energy on the main slip plane [110] compared to predictions of density-functional theory [54, 55]. This is directly related to homogenous dislocation nucleation while a cutting process may also show heterogenous dislocations. This in theory means that there is a remote possibility that the dislocations observed in the simulation were less mobile than in reality. However, this aspect would have contributed equally both to conventional cutting and EVAM simulation and therefore, the results reported here are insensitive to the overestimated fault energy of the ABOP.

4.2. Analysis of cutting chips

Figure 5 sheds light on the analysis of the cutting chips. The analysis was accompanied by employing the Polyhedral template matching (PTM) method to probe the localized changes in the crystal structure occurring during the cutting process. PTM is a structure identification method [56] promising reliability over other identification methods like Common Neighbor Analysis (CNA), typically in a scenario of cutting or indentation whereby atoms undergo strong thermal fluctuations and high strains. Furthermore, it provides a direct calculation of the local (per-atom) orientation, elastic deformation, strain and alloy type. The processed results, shown in figure 5, highlight the differences in the chip morphology, cut chip thickness, as well as the local measures of stress and temperature in the deformation zone.

Figure 5 shows processed results wherein an atom count was performed to quantify the number of BCC atoms (blue coloured), FCC atoms (green coloured), HCP atoms (red coloured) and several unidentified atoms (white coloured with the exception that the diamond tool was not part of this analysis and hence shown white in colour). An immediate difference in the chip morphology and the crystal structure of the cutting chips is evident from this analysis.

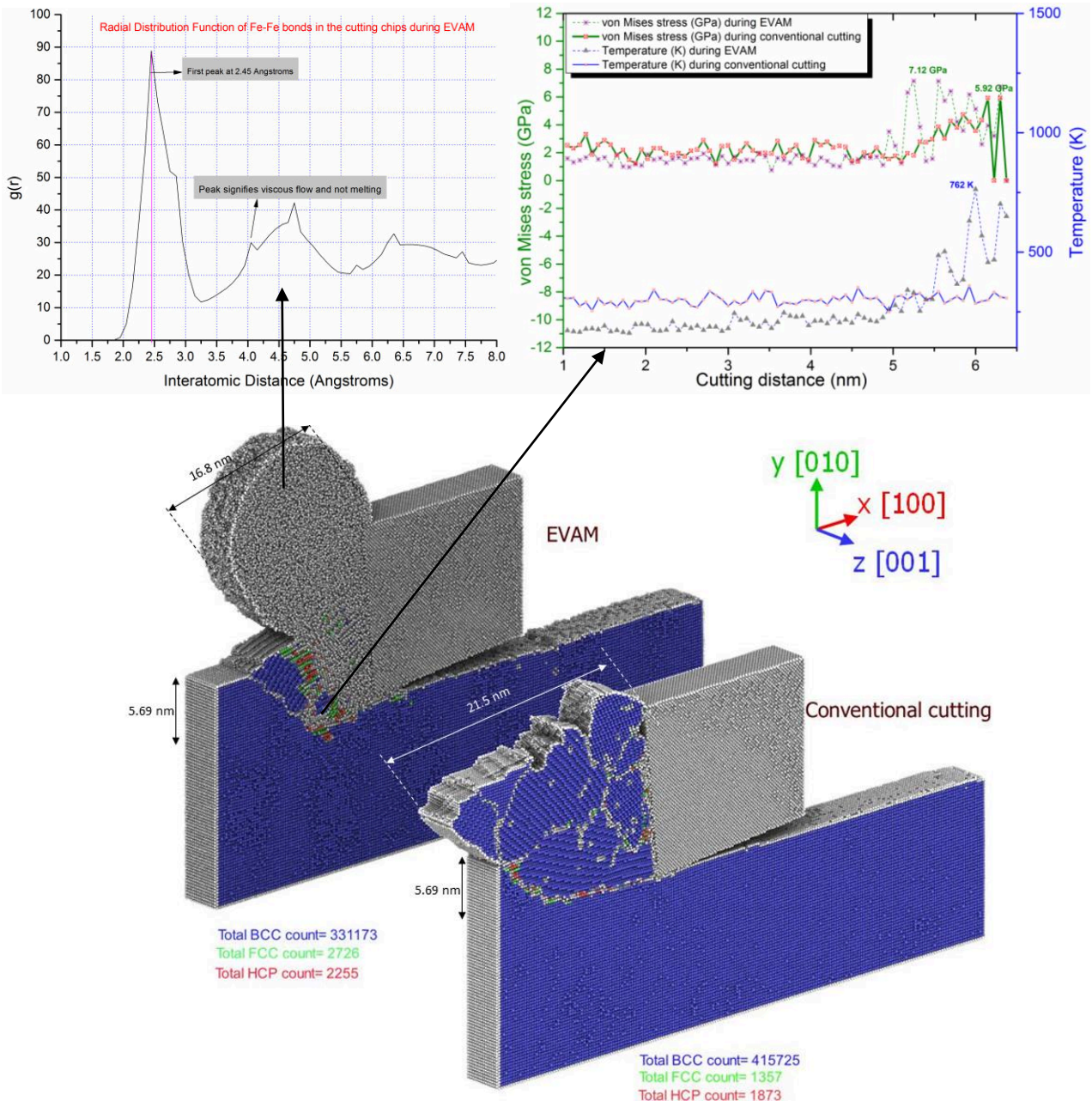

Figure 5: Comparison of chip morphology and local changes in the crystal structure during conventional cutting and EVAM. Colours represent local crystal structure identified by the Polyhedral matching algorithm. The comparison of EVAM also shows the cutting chip thickness measured as well as the radial distribution function of the localised cutting chips and the von Mises stress peak and temperature peak in the deformation zone of iron workpiece

Table IX: Comparison of chip morphology and chip thickness ratio

Machining condition	Uncut chip thickness	Cut chip thickness	Ratio of uncut chip thickness to cut chip thickness (r)	Nature of the cutting chip
Conventional cutting	5.69 nm	21.5 nm	0.26	Shear slip generated small crystallites of iron separated by grain boundaries
EVAM	5.69 nm	16.8 nm	0.34	Viscous plastic flow with severe structural disordering

A quantification of the uncut chip thickness and chip thickness ratio shown in Table IX confirms the experimental finding the EVAM process results in thinning of cutting chips and thereby an increase in the ratio of the uncut chip thickness to cut chip thickness. The number of BCC atoms during conventional cutting were found to be higher than in the EVAM process highlighting that the cutting chips during EVAM process lost their structural order completely as opposed to conventional cutting in which the chips become polycrystalline and still retain their crystal structure.

Next, the stress and temperature were measured concurrently during the cutting process as shown in the top part of figure 5. It shows that the von Mises stress was roughly of the same order but the temperature in the cutting zone was significantly higher during EVAM compared to conventional cutting. The magnitude of peak temperature observed from the simulations during the yielding process was less than 1000 K, thereby ruling out the possibility of melting of iron. To investigate this further, a radial distribution of the cutting chips of iron during EVAM was taken as highlighted in the top left portion of figure 5. Evidence reported in the literature suggests that the presence of the peak in the second order of the RDF indicates shear induced plastic viscous flow of iron with some order of crystallinity [57]. The distance between the other higher order peaks correspond to the distance between the [-110] plane of the BCC iron. This information can be used to infer that the process of EVAM induces better viscous flow and thus ductile plasticity in iron compared to conventional cutting. Most noticeably, it highlights that the degree of high plasticity or higher plastic flow during EVAM or iron is not by virtue of dislocation nucleation but rather shear vibration induced viscous plastic flow of BCC iron.

4.3. Difference in tool wear during conventional cutting and EVAM

Figure 6 presents a comparison of the cutting tool analysed from the molecular dynamics simulation. The analysis made use of the identify diamond lattice structure module, which highlights blue atoms in their perfectly bonded sp^3 state. The green atoms are surface atoms on the diamond tool whilst pink atoms are those atoms which have lost their original bonding

configuration and symbolise initiation of the diamond tool wear. As the cutting length in the simulation was rather small, the simulation results did not show the tool atoms completely detached. However, a noticeable difference of the surface topology was observed on the rake face and the flank face of the tool.

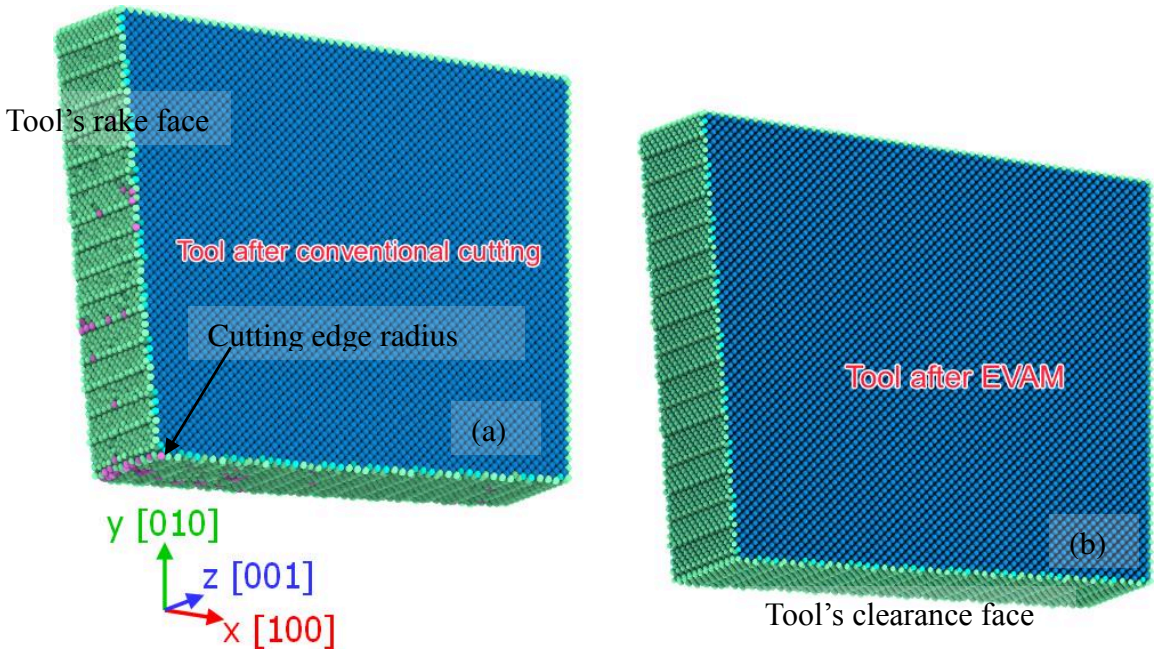

Figure 6: Post-machining image of the tool after (a) conventional cutting (b) using EVAM

The wear mechanism is still being examined (we aim to expand on this in future), but surface initiated wear can be seen to occur during conventional cutting but not during EVAM. It highlights another advantage of EVAM, that it could enhance wear protection for the diamond tool as opposed to conventional cutting.

6. Conclusions

Precision micromachining of low carbon ferrous alloys has been a long-sought goal of precision engineering research. In the recent past, the elliptical vibration assistance machining (EVAM) approach wherein the toolpath is modified by oscillating the diamond tool is experimentally reported to be beneficial for tool life and to achieve nanometric finish on steel workpieces. However, a good theoretical understanding for this outcome is lacking. The paper revisits the conventional cutting process and compares it with the EVAM process. The pilot implementation was done via the development of a molecular dynamics simulation model of cutting pure iron using

an analytical bond order potential function that is fully parametrised both for iron and carbon. Based on the discussion, the answers to the initial four open questions can be summarised as follows:

1. Conventional cutting and EVAM approaches showed distinct features in the formation of the cutting chips and the way in which the plasticity evolves during the process. The EVAM process showed thinning of cutting chips resulting in an increase in the ratio of uncut chip thickness to cut chip thickness.
2. The cutting forces and the coefficient of kinetic friction during the EVAM process are far lower than in the conventional cutting process, whereas the temperature in the cutting zone during the EVAM process is higher than in the conventional cutting process.
3. The radial distribution function of the cutting chips suggests that the nature of cutting chips is plastically viscous with a flow property much better during the EVAM process than in the conventional cutting process. The ductile plasticity during conventional cutting was due to dislocation nucleation and propagation of type **b**=1/2<111>, **b**=<100> and **b**=<110> ultimately resulting in crystallites of iron separated by grain boundaries. Contrary to this, the transport of plasticity during EVAM was largely observed due to the viscous flow with minor evidence of the presence of dislocations of type **b**=1/2<111>. Consequently, the cutting chips during conventional cutting are crystalline in nature, separated by granular boundaries while the nature of cutting chips during the EVAM process showed a severe degree of disordering.
4. The surface initiated wear on the diamond tool was present only during the conventional cutting and not during the EVAM process. This observation highlights the wear protection advantages associated with the use of EVAM while using the diamond tool against ferrous alloys.

Acknowledgments:

This work was done in the Doctoral Training Centre (DTC) in Ultra-Precision at Cranfield University which is supported by the RCUK *via* Grant No.: EP/K503241/1. Author’s acknowledges help of Dr Michael Knaggs for accessing Cranfield’s Delta HPC service as well as PRACE for granting access to HLRS resource based in Germany at Stuttgart. SG would also like to acknowledge the financial support from the COST Action CA15102 in undertaking this work.

References

[1] E. Brinksmeier, W. Preuss, Micro-machining, Philosophical Transactions of the Royal Society A: Mathematical, Physical and Engineering Sciences 370(1973) (2012) 3973-3992.
[2] S. Goel, X. Luo, A. Agrawal, R.L. Reuben, Diamond machining of silicon: A review of advances in molecular dynamics simulation, International Journal of Machine Tools and Manufacture 88(0) (2015) 131-164.
[3] C.J. Evans, J.B. Bryan, “Structured”,“textured” or “engineered” surfaces, Cirp Ann-Manuf Techn 48(2) (1999) 541-556.
[4] C.J. Evans, Precision engineering: an evolutionary perspective, Philosophical Transactions of the Royal Society A: Mathematical, Physical and Engineering Sciences 370(1973) (2012) 3835-3851.
[5] N. Ikawa, T. Tanaka, Thermal aspects of wear of diamond grain in grinding, Annals of the CIRP 19(1) (1971) 153-157.
[6] S. Goel, A topical review on "The current understanding on the diamond machining of silicon carbide", Journal of Physics D: Applied Physics 47(24) (2014) 243001.
[7] E. Paul, C.J. Evans, A. Mangamelli, M.L. McGlauflin, R.S. Polvani, Chemical aspects of tool wear in single point diamond turning, Precision Engineering 18(1) (1996) 4-19.
[8] R. Komanduri, M.C. Shaw, Wear of synthetic diamond when grinding ferrous metals, Nature 255(5505) (1975) 211-213.
[9] R. Narulkar, S. Bukkapatnam, L.M. Raff, R. Komanduri, Graphitization as a precursor to wear of diamond in machining pure iron: A molecular dynamics investigation, Comp Mater Sci 45(2) (2009) 358-366.
[10] S.Z. Chavoshi, S. Goel, P. Morantz, Current trends and future of sequential micro-machining processes on a single machine tool, Mater Design 127 (2017) 37-53.
[11] S.Z. Chavoshi, X. Luo, Hybrid micro-machining processes: A review, Precision Engineering 41(Supplement C) (2015) 1-23.
[12] Y. He, P. Zou, W.-L. Zhu, K.F. Ehmann, Ultrasonic elliptical vibration cutting of hard materials: simulation and experimental study, The International Journal of Advanced Manufacturing Technology 91(1-4) (2017) 363-374.
[13] H. Sui, X. Zhang, D. Zhang, X. Jiang, R. Wu, Feasibility study of high-speed ultrasonic vibration cutting titanium alloy, J Mater Process Tech 247(Supplement C) (2017) 111-120.
[14] B. Bulla, F. Klocke, O. Dambon, M. Hünten, Ultrasonic assisted diamond turning of hardened steel for mould manufacturing, Key Engineering Materials, Trans Tech Publ, 2012, pp. 437-442.
[15] R. Singh, J. Khamba, Ultrasonic machining of titanium and its alloys: a review, J Mater Process Tech 173(2) (2006) 125-135.
[16] V. Sharma, P.M. Pandey, Recent advances in ultrasonic assisted turning: A step towards sustainability, Cogent Engineering 3(1) (2016) 1222776.
[17] G.D. Kim, B.G. Loh, Characteristics of chip formation in micro V-grooving using elliptical vibration cutting, J Micromech Microeng 17(8) (2007) 1458.

[18] T. Moriwaki, E. Shamoto, Ultraprecision Diamond Turning of Stainless Steel by Applying Ultrasonic Vibration, CIRP Annals - Manufacturing Technology 40(1) (1991) 559-562.
[19] T. Moriwaki, E. Shamoto, Ultrasonic elliptical vibration cutting, Cirp Ann-Manuf Techn 44(1) (1995) 31-34.
[20] E. Shamoto, T. Moriwaki, Ultaprecision Diamond Cutting of Hardened Steel by Applying Elliptical Vibration Cutting, CIRP Annals - Manufacturing Technology 48(1) (1999) 441-444.
[21] C. Ma, E. Shamoto, T. Moriwaki, Y. Zhang, L. Wang, Suppression of burrs in turning with ultrasonic elliptical vibration cutting, International Journal of Machine Tools and Manufacture 45(11) (2005) 1295-1300.
[22] E. SHAMOTO, Simulation of elliptical vibration cutting process with thin shear plane model, Proc ASPE, 2007, pp. 64-69.
[23] V. Astashev, V. Babitsky, Ultrasonic cutting as a nonlinear (vibro-impact) process, Ultrasonics 36(1-5) (1998) 89-96.
[24] E. Brinksmeier, R. Glabe, Elliptical vibration cutting of steel with diamond tools, Proc. of the 14th Annual ASPE Meeting, Monterey, California, USA, 1999.
[25] Y. Yang, Y. Pan, P. Guo, Structural coloration of metallic surfaces with micro/nano-structures induced by elliptical vibration texturing, Appl Surf Sci 402 (2017) 400-409.
[26] R. Muhammad, M.S. Hussain, A. Maurotto, C. Siemers, A. Roy, V.V. Silberschmidt, Analysis of a free machining α+ β titanium alloy using conventional and ultrasonically assisted turning, J Mater Process Tech 214(4) (2014) 906-915.
[27] R. Muhammad, A. Maurotto, M. Demiral, A. Roy, V.V. Silberschmidt, Thermally enhanced ultrasonically assisted machining of Ti alloy, CIRP Journal of Manufacturing Science and Technology 7(2) (2014) 159-167.
[28] S. Patil, S. Joshi, A. Tewari, S.S. Joshi, Modelling and simulation of effect of ultrasonic vibrations on machining of Ti6Al4V, Ultrasonics 54(2) (2014) 694-705.
[29] A. Maurotto, R. Muhammad, A. Roy, V. Babitsky, V. Silberschmidt, Comparing machinability of Ti-15-3-3-3 and Ni-625 alloys in UAT, Procedia CIRP 1 (2012) 330-335.
[30] C. Nath, M. Rahman, S. Andrew, A study on ultrasonic vibration cutting of low alloy steel, J Mater Process Tech 192 (2007) 159-165.
[31] J. Zhang, T. Cui, C. Ge, Y. Sui, H. Yang, Review of micro/nano machining by utilizing elliptical vibration cutting, International Journal of Machine Tools and Manufacture 106 (2016) 109-126.
[32] Y. Liang, D. Li, Q. Bai, S. Wang, M. Chen, Molecular Dynamics Simulation of Elliptical Vibration Cutting, Nano/Micro Engineered and Molecular Systems, 2006. NEMS'06. 1st IEEE International Conference on, IEEE, 2006, pp. 635-638.
[33] B. Zhu, D. Zhao, H. Zhao, J. Guan, P. Hou, S. Wang, L. Qian, A study on the surface quality and brittle–ductile transition during the elliptical vibration-assisted nanocutting process on monocrystalline silicon via molecular dynamic simulations, RSC Advances 7(7) (2017) 4179-4189.
[34] Y. Gao, C.J. Ruestes, H.M. Urbassek, Nanoindentation and nanoscratching of iron: Atomistic simulation of dislocation generation and reactions, Comp Mater Sci 90(0) (2014) 232-240.
[35] N. Gunkelmann, I. Alabd Alhafez, D. Steinberger, H.M. Urbassek, S. Sandfeld, Nanoscratching of iron: A novel approach to characterize dislocation microstructures, Comp Mater Sci 135(Supplement C) (2017) 181-188.
[36] A. AlMotasem, J. Bergström, A. Gåård, P. Krakhmalev, L. Holleboom, Atomistic Insights on the Wear/Friction Behavior of Nanocrystalline Ferrite During Nanoscratching as Revealed by Molecular Dynamics, Tribology letters 65(3) (2017) 101.
[37] S. Plimpton, Fast Parallel Algorithms for Short-Range Molecular Dynamics, J Comput Phys 117 (1995) 1-19.
[38] A. Stukowski, Visualization and analysis of atomistic simulation data with OVITO–the Open Visualization Tool, Model Simul Mater Sc 18(1) (2010).
[39] A. Stukowski, V.V. Bulatov, A. Arsenlis, Automated identification and indexing of dislocations in crystal interfaces, Model Simul Mater Sc 20(8) (2012) 085007.

[40] A. Stukowski, K. Albe, Extracting dislocations and non-dislocation crystal defects from atomistic simulation data, Model Simul Mater Sc 18(8) (2010) 085001.
[41] K.O.E. Henriksson, K. Nordlund, Simulations of cementite: An analytical potential for the Fe-C system, Phys Rev B 79(14) (2009) 144107.
[42] K.O.E. Henriksson, C. Björkas, K. Nordlund, Atomistic simulations of stainless steels: a many-body potential for the Fe–Cr–C system, Journal of Physics: Condensed Matter 25(44) (2013) 445401.
[43] D.J. Hepburn, G.J. Ackland, Metallic-covalent interatomic potential for carbon in iron, Phys Rev B 78(16) (2008) 165115.
[44] B.J. Lee, A modified embedded-atom method interatomic potential for the Fe-C system, Acta Mater 54(3) (2006) 701-711.
[45] J.A. Rayne, B.S. Chandrasekhar, Elastic Constants of Iron from 4.2 to 300K, Physical Review 122(6) (1961) 1714-1716.
[46] S. Goel, A. Stukowski, X. Luo, A. Agrawal, R.L. Reuben, Anisotropy of single-crystal 3C–SiC during nanometric cutting, Model Simul Mater Sc 21(6) (2013) 065004.
[47] V.I. Yamakov, D.H. Warner, R.J. Zamora, E. Saether, W.A. Curtin, E.H. Glaessgen, Investigation of crack tip dislocation emission in aluminum using multiscale molecular dynamics simulation and continuum modeling, J Mech Phys Solids 65(0) (2014) 35-53.
[48] R. Hill, The Elastic Behaviour of a Crystalline Aggregate, Proceedings of the Physical Society. Section A 65(5) (1952) 349.
[49] M. Michael, E. Paul, A. Karsten, Analytic bond-order potential for bcc and fcc iron—comparison with established embedded-atom method potentials, Journal of Physics: Condensed Matter 19(32) (2007) 326220.
[50] C. Björkas, K. Nordlund, Comparative study of cascade damage in Fe simulated with recent potentials, Nuclear Instruments and Methods in Physics Research Section B: Beam Interactions with Materials and Atoms 259(2) (2007) 853-860.
[51] M. Melnykov, PhD thesis on Solid-Liquid Interfacial Properties of Fe and Fe-C Alloys from Molecular Dynamics Simulations, University of Leicester, 2013.
[52] S. Goel, S.S. Joshi, G. Abdelal, A. Agrawal, Molecular dynamics simulation of nanoindentation of Fe3C and Fe4C, Materials Science and Engineering: A 597(0) (2014) 331-341.
[53] S. Goel, A. Kovalchenko, A. Stukowski, G. Cross, Influence of microstructure on the cutting behaviour of silicon, Acta Mater 105 (2016) 464-478.
[54] M. Müller, P. Erhart, K. Albe, Analytic bond-order potential for bcc and fcc iron—comparison with established embedded-atom method potentials, Journal of Physics: Condensed Matter 19(32) (2007) 326220.
[55] J.-A. Yan, C.-Y. Wang, S.-Y. Wang, Generalized-stacking-fault energy and dislocation properties in bcc Fe: A first-principles study, Physical Review B 70(17) (2004) 174105.
[56] P.M. Larsen, S. Schmidt, J. Schiøtz, Robust structural identification via polyhedral template matching, Model Simul Mater Sc 24(5) (2016) 055007.
[57] C.J. Wu, P. Söderlind, J.N. Glosli, J.E. Klepeis, Shear-induced anisotropic plastic flow from body-centred-cubic tantalum before melting, Nat Mater 8(3) (2009) 223-228.

2018-05-23

Molecular dynamics simulation of the elliptical vibration-assisted machining of pure iron

Goel, Saurav

SAGE

Goel S, Duarte Martinez F, Chavoshi SZ, et al., (2018) Molecular dynamics simulation of the elliptical vibration-assisted machining of pure iron. Journal of Micromanufacturing, Volume 1, Issue 1, May 2018, pp. 6-19

http://dx.doi.org/10.1177/2516598418765359